KSME

Springer

Journal of Mechanical Science and Technology 34 (3) 2020

Original Article
DOI 10.1007/s12206-020-0202-8

Keywords:
· Accuracy analysis
· Bearing clearances
· Multi-loop mechanism
· Spatial revolute joint

Correspondence to:
Chuanzhi Chen
czchen_nuaa@163.com

Citation:
Lin, F., Chen, C., Chen, J., Chen, M. (2020). Accuracy analysis of spatial multi-loop mechanism effected by paired bearings support joint clearance. Journal of Mechanical Science and Technology 34 (3) (2020) 987~1003.
http://doi.org/10.1007/s12206-020-0202-8

Received July 9th, 2019
Revised January 9th, 2020
Accepted January 14th, 2020

† Recommended by Editor
No-cheol Park

Accuracy analysis of spatial multi-loop mechanism effected by paired bearings support joint clearance

Fei Lin[1], Chuanzhi Chen[1], Jinbao Chen[1] and Meng Chen[2]

[1]College of Astronautics, Nanjing University of Aeronautics and Astronautics, Nanjing 210016, China, [2]Aerospace Systems Engineering Shanghai, Shanghai 201108, China

Abstract The primary objective of this work is to present a three-dimensional (3D) clearance model of the paired bearings support joint (PBS-joint) and address the influence of PBS-joint clearance on the accuracy of the spatial multi-loop mechanism. Through the synthetic use of the vector and homogeneous coordinate transformation methods, the 3D clearance model of the PBS-joint is obtained on the basis of the static balance condition. When clearance is equated as a spatial virtual link, the error space solution models of serial mechanism and single-loop mechanism are developed respectively according to the Denavit-Hartenberg method and the geometric closure condition. The error space standardization solution model of the multi-loop mechanism is then presented through improving the low-layer loop sequence description method of the topological structure relations. Finally, the application in the basic loop mechanism is demonstrated to discuss the procedures adopted in this work and the influence of the PBS-joint clearance. Results show that the PBS-joint clearance may cause the error on the point with a 3D deviation transmission path to deviate the normal distribution. Moreover, the plane-joint clearance model may not yield an accurate analysis of the spatial mechanism.

1. Introduction

In mechanical systems, the revolute joint usually adopts the structure of two deep groove ball bearings supporting shaft to reduce friction and improve bearing capacity. This type of revolute joint is referred to as paired bearings support joint (PBS-joint). Fig. 1 shows the assembly relationships between PBS-joint and links. Two deep groove ball bearings are installed at both ends of the shaft, the outer rings of the bearings are fixed with link *j*, the inner rings of the bearings are fixed with the shaft, and the shaft is fixed with link *j*+1.

The internal structure of a PBS-joint is shown in Fig. 2. The inner and outer rings come into contact indirectly through the ball. Their relative motion is limited by the geometric characteristics of the inner raceway, ball, and outer raceway. The absence of clearance in bearings causes the shaft to rotate only around its own axis. The relative motion of the components connected by PBS-joint has no deviation. However, when the bearings have radial clearance (G_r), the shaft can either deflect relative to the outer ring or move along the radial and axial directions. As a result, the relative motion of components connected by the PBS-joint becomes uncertain, and the positional accuracy of the mechanism is affected. For robots, solar panels, spaceborne antennas, space telescopes, and other equipment, positional accuracy is often the key factor to ensure the normal operation of the system [1-5]. Such equipment also need the high accuracy spatial multi-loop mechanism to deal with complex tasks [6-10]. In reality, the bearing clearance cannot be ignored in meeting the requirements of movement and assembly. Therefore, to improve and control the mechanism accuracy, the influence of PBS-joint clearance on mechanism accuracy, especially on spatial multi-loop mechanism, should be analyzed.

In the course of studying the effects of revolute joint clearance on the mechanism, researchers have proposed several clearance models. These models can be classified by spatial

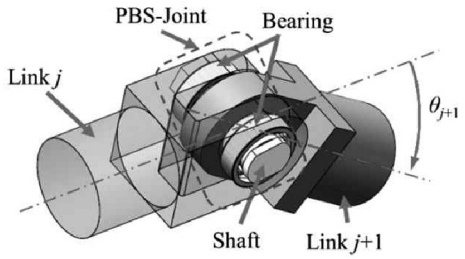

Fig. 1. Links connected by PBS-joint.

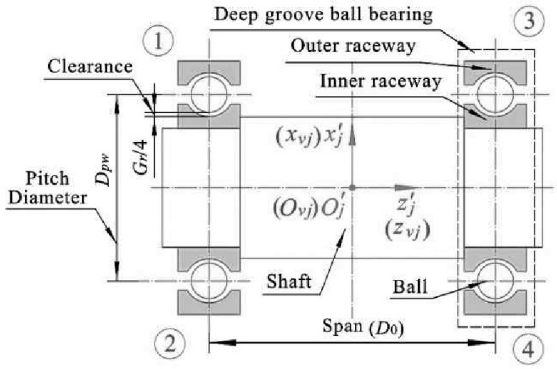

Fig. 2. Construction of PBS-joint.

dimension as (1) plane revolute joint (plane-joint) clearance model with only radial deviation considered [11-14], (2) cylindrical joint clearance model with both deflection and radial deviation considered [15-19], and (3) spatial revolute joint clearance model with all the deflection, radial, and axial deviation considered [20-22]. When only the radial deviation is considered, the deviation of the inner ring relative to the outer ring is similar to the hole-shaft model [11], and the PBS-joint clearance can be described by the plane-joint clearance model. However, this model is only suitable for the accuracy analysis of the plane mechanism. For the spatial mechanism, the influence of three-dimensional (3D) deviation caused by the joint clearance should be taken into account. Although the second and third kinds of clearance models can reflect the 3D deviation, their compositions comprise the cylinder shell and shaft, which are significantly different from the geometric construction of the PBS-joint. Thus, these models are not suitable.

In addition, the analysis of the mechanism accuracy effected by joint clearance is a complicated process. At present, most studies are focused on non-redundant mechanisms, such as serial [1, 23-27], single-loop [28-38], and general parallel mechanisms [2, 39-43]. The nonlinear behaviors and energy balance of the joint within high dynamic conditions are studied [19, 44]. For multi-loop mechanisms that contain a complex interloop constraint relationship and numerous redundant constraints, the relationships between joint clearance and component pose are highly nonlinear and coupled, and the accuracy analysis may be very difficult. Nevertheless, some scholars have attempted to solve this problem and have achieved some breakthrough results. For instance, Tsai et al. [45] presented a general analytical method for multi-loop mechanism accuracy by using the transmission wrench screw and joint twist screw. Although the accuracy can be solved theoretically using this method, establishing and solving the constraint equation when many closed loops and complex coupled relationship between loops exist are difficult. Erkaya [46] studied the trajectory optimization of a multi-loop mechanism with joint clearance. Zhang et al. [47-48] addressed the accuracy influence of redundancy constraint on a planar parallel mechanism with clearance and presented an approach to improve accuracy by using a redundant actuator. Lin et al. [49] studied the effect of force on joint clearance distribution of the multi-loop deployable mechanism. Li et al. [50] and Zhao et al. [51] analyzed the angular error of the multi-loop mechanism caused by joint clearance. Meanwhile, Zhao et al. [14] also studied the relationship between joint clearance and assembly accuracy of the multi-loop mechanism and proposed an algorithm to predict the precision of the mechanism. Akhadkar et al. [22] studied the effect of 3D revolute joint clearance on force transmission of the multi-loop mechanism. In the above studies, the transmission priority of deviation assumed that the deviation was transmitted from the single loop near the reference frame or driven to the single loop far away. On the basis of this assumption, the deviation poses of each single loop can be determined one by one and then the accuracy of the multi-loop mechanism can be solved. However, the general law of deviation transmission has not been presented, which may be difficult to obtain directly in a complex multi-loop mechanism. Zhao et al. [52] pointed out the law of deviation transmission by studying the relationship between mechanism assembly process and deviation transmission. However, the literature only illustrated the priority of deviation transmission through examples. The definition and calculation method of distance from single loops to frame or actuator were not clearly shown. Therefore, the description of deviation transmission characteristics is still unclear.

To obtain the accuracy evaluation results that are close to the actual situation and solve the problems existing in the accuracy analysis of the multi-loop mechanism, this study is presented in three parts. In Sec. 2, a 3D clearance model that considers the shaft deflection and radial and axial deviations is presented according to the geometric characteristics of PBS-joint. In Sec. 3, the deviation transmission model between components is established by equating the PBS-joint clearance as a spatial virtual link, and a standard accuracy analysis method for the multi-loop mechanism is presented. In Sec. 4, a case is presented to reveal the influence law of PBS-joint clearance on the accuracy of the spatial multi-loop mechanism.

2. PBS-joint clearance model

The geometric parameters of the two bearings in one PBS-joint are assumed to be the same in this work.

2.1 Description of static deviation pose

All PBS-joints should be in the stable load-bearing configuration when the mechanism is in static balance. According to force balance theory and the geometric characteristics shown in Fig. 2, to obtain a PBS-joint with stable load-bearing configuration, at least two points of ①-④ should be in the stable load-bearing configuration. Specifically, the inner and outer raceways are in contact with the ball in the same time and their center points are collinear.

The static balanced PBS-joint can be divided into two types according to whether the shaft axis is deflected from the bearing outer ring axis, namely, offset static (the shaft axis is parallel to the axis of the outer ring) and deflection static (the shaft axis intersects with the axis of the outer ring). To describe the shaft pose in PBS-joint, a fixed reference frame $O_j^{'}-x_j^{'}y_j^{'}z_j^{'}$ is set at the center point of the center surface defined by the outer rings of the two bearings, and a moving reference frame $O_{vj}-x_{vj}y_{vj}z_{vj}$ is set at the center of the shaft. The axes $x_j^{'}$ and x_{vj} are along the radial directions of the outer ring and shaft, respectively, and the axes $z_j^{'}$ and z_{vj} are along the axis directions. The directions of axes $y_j^{'}$ and y_{vj} are determined by the right-hand law. To distinguish the shaft poses in different states, reference frames $O^P-x^Py^Pz^P$ and $O^R-x^Ry^Rz^R$ are adopted to denote the reference frame $O_{vj}-x_{vj}y_{vj}z_{vj}$ in the offset static and deflection static, respectively, as shown in Figs. 3 and 4.

The possible states of bearings on both sides in PBS-joint are symmetrical about axis $z_j^{'}$ and plane $O_j^{'}-x_j^{'}y_j^{'}$ in 3D space. Therefore, if the static deviation poses of the shaft can be determined in the case where one of the bearings at position ①-④ is in the stable load-bearing configuration, then, by converting it into 3D space, all of the static deviation poses of the shaft will be obtained. In this study, the position ③ is taken into consideration in the analysis.

When the PBS-joint is in the offset static, the balls at position ① and ③ are compressed and the bearings form a stable load-bearing configuration (Fig. 3). According to the forming conditions of the stable load-bearing configuration, the following relationships can be obtained:

$$\begin{cases} r^x_{O_{e3}O_{i3}} = S_G - \left(\dfrac{G_r}{2} - r^x_{O^P}\right), \\ r^z_{O_{e3}O_{i3}} = r^z_{O^P} \end{cases} \tag{1}$$

where O_{in}, O_{en}, and O_{wn} ($n=1,2,3,4$) are the centers of the inner raceway, outer raceway, and ball, respectively. The coefficient $\boldsymbol{r}_{ab}$ denotes the vector from a to b in $O_j^{'}-x_j^{'}y_j^{'}z_j^{'}$. If points a and b coincide, then a is omitted and expressed as $\boldsymbol{r}_b$. The coefficient r^k_{ab} denotes the k direction component of $\boldsymbol{r}_{ab}$, $k=x,y,z$ and $r^x_{O^P}\in\left[0,\dfrac{G_r}{2}\right]$, and G_r denotes the radial clearance of bearing. In the equation $S_G=R_i+R_e-D_w$, R_i denotes the radius of the inner raceway, R_e denotes the radius of the outer raceway, and D_w denotes the diameter of the ball.

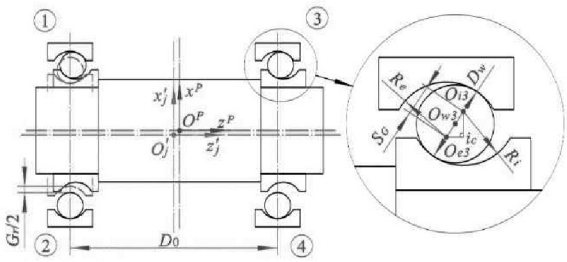

Fig. 3. PBS-joint in offset static.

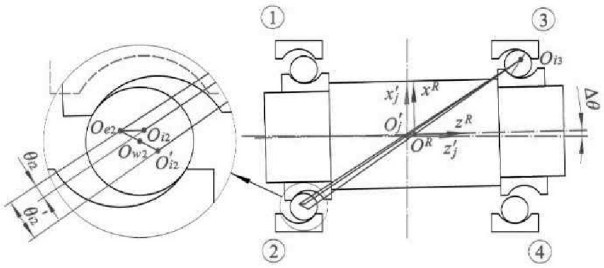

Fig. 4. PBS-joint in deflection static.

In $\Delta i_c O_{e3} O_{i3}$, the following geometrical relationship can be obtained as follows:

$$\left(r^z_{O^P}\right)^2 = S_G^2 - \left[S_G - \left(\frac{G_r}{2} - r^x_{O^P}\right)\right]^2. \tag{2}$$

Thus, the relationship between axial and radial offset is

$$r^z_{O^P} = \pm\frac{\sqrt{\left(G_r - 2r^x_{O^P}\right)\left(4S_G - G_r + 2r^x_{O^P}\right)}}{2}. \tag{3}$$

In addition, when the radial offset reaches the maximum value $\dfrac{G_r}{2}$, the axial offset is zero. When the radial offset is zero, the axial offset reaches the maximum value where the balls at position ①-④ are compressed at the same time.

When the PBS-joint is in the deflection static, the balls at position ② and ③ are compressed, and the bearings form a stable load-bearing configuration (Fig. 3). To determine the shaft pose in deflection static, the shaft is assumed to be first moved into offset static ($O_{vj}-x_{vj}y_{vj}z_{vj}$ is denoted as $O^P-x^Py^Pz^P$), and then rotated into the deflection static ($O_{vj}-x_{vj}y_{vj}z_{vj}$ is denoted as $O^R-x^Ry^Rz^R$). The rotation center is the center of any inner raceway in the stable load-bearing configuration. In particular, the shaft in deflection static without a deviated shaft center (i.e., O_{vj} coincides with $O_j^{'}$) is only the special case wherein the shaft center is deviated during the moving process. However, the shaft is returned to its original

position in the process of rotating. Fig. 4 is the deflection static obtained by rotating the shaft in offset static, as shown in Fig. 3, where the rotation center is O_{i3} (the inner raceway center at position ③).

In the initial state (Fig. 1), the vector of each point in the reference frame $O_j^{'}-x_j^{'}y_j^{'}z_j^{'}$ is

$$\begin{cases} {}^{o}\boldsymbol{r}_{O_{i3}}=\left[\dfrac{D_{pw}}{2}-\dfrac{D_w}{2}-\dfrac{G_r}{4}+R_i,\ 0,\ \dfrac{D_0}{2}\right]^T \\ {}^{o}\boldsymbol{r}_{O_{i2}}=\left[-\left(\dfrac{D_{pw}}{2}-\dfrac{D_w}{2}-\dfrac{G_r}{4}+R_i\right),\ 0,\ -\dfrac{D_0}{2}\right]^T \\ {}^{o}\boldsymbol{r}_{O_{e2}}=\left[-\left(\dfrac{D_{pw}}{2}+\dfrac{D_w}{2}+\dfrac{G_r}{4}-R_e\right),\ 0,\ -\dfrac{D_0}{2}\right]^T \end{cases} \tag{4}$$

where D_{pw} is the diameter of the bearing pitch circle, and D_0 is the support span of the shaft (i.e., the distance between the center faces of the two supporting bearings).

In the deflection static (Fig. 3), the vectors have been changed and could be described as

$$\begin{cases} \boldsymbol{r}_{O_{i3}}={}^{o}\boldsymbol{r}_{O_{i3}}+\boldsymbol{r}_{O^P} \\ \boldsymbol{r}_{O_{i2}}={}^{o}\boldsymbol{r}_{O_{i2}}+\boldsymbol{r}_{O^P} \\ \boldsymbol{r}_{O_{e2}}={}^{o}\boldsymbol{r}_{O_{e2}} \end{cases}. \tag{5}$$

From offset static (Fig. 3) to deflection static (Fig. 4), the positions of O_{i3} and O_{e2} remain unchanged, whereas O_{i2} is offset to $O_{i2}^{'}$. Thus,

$$\left\|\boldsymbol{r}_{O_{i2}^{'}O_{i3}}\right\|=\left\|\boldsymbol{r}_{O_{i2}O_{i3}}\right\|, \tag{6}$$

where $\|\boldsymbol{r}_{ab}\|=\sqrt{\boldsymbol{r}_{ab}^T\boldsymbol{r}_{ab}}$.

According to the stable load-bearing configuration of bearings, the following relationship can be obtained:

$$\left\|\boldsymbol{r}_{O_{e2}O_{i2}^{'}}\right\|=S_G. \tag{7}$$

In $\Delta O_{i3}O_{e2}O_{i2}^{'}$, $\theta_{i2}^{'}$ can be obtained by the law of cosines, described as

$$\theta_{i2}^{'}=\arccos\frac{\left\|\boldsymbol{r}_{O_{e2}O_{i3}}\right\|^2+\left\|\boldsymbol{r}_{O_{i2}^{'}O_{i3}}\right\|^2-\left\|\boldsymbol{r}_{O_{e2}O_{i2}^{'}}\right\|^2}{2\left\|\boldsymbol{r}_{O_{e2}O_{i3}}\right\|\left\|\boldsymbol{r}_{O_{i2}^{'}O_{i3}}\right\|}. \tag{8}$$

Moreover, in $\Delta O_{i3}O_{e2}O_{i2}$, θ_{i2} can be obtained and described as

$$\theta_{i2}=\arccos\frac{\left\|\boldsymbol{r}_{O_{e2}O_{i3}}\right\|^2+\left\|\boldsymbol{r}_{O_{i2}O_{i3}}\right\|^2-\left\|\boldsymbol{r}_{O_{e2}O_{i2}}\right\|^2}{2\left\|\boldsymbol{r}_{O_{e2}O_{i3}}\right\|\left\|\boldsymbol{r}_{O_{i2}O_{i3}}\right\|}. \tag{9}$$

If the vector $\boldsymbol{r}_S$ is defined as

$$\boldsymbol{r}_S=\boldsymbol{r}_{O_{e2}O_{i3}}\times\boldsymbol{r}_{O_{e2}O_{i2}}, \tag{10}$$

then the angle between z^R and $z_j^{'}$ can be calculated as

$$\Delta\theta=\theta_{i2}^{'}+Sn\theta_{i2}, \tag{11}$$

where $Sn=\boldsymbol{e}_S^T\boldsymbol{e}_y$, $\boldsymbol{e}_k$, $k=x,y,z$ is the base vector of the Cartesian coordinate system, and $\boldsymbol{e}_S=\dfrac{\boldsymbol{r}_S}{\sqrt{\boldsymbol{r}_S^T\boldsymbol{r}_S}}$ is the base vector of $\boldsymbol{r}_S$.

According to the vector angle formula, the angle between vector $\boldsymbol{r}_{O_{i2}O_{i3}}$ and axis $z_j^{'}$ can be determined as follows:

$$\theta_z=\arccos\frac{\boldsymbol{r}_{O_{i2}O_{i3}}^T\boldsymbol{e}_z}{\left\|\boldsymbol{r}_{O_{i2}O_{i3}}\right\|}. \tag{12}$$

As previously assumed, the shaft in the deflection static is obtained by rotating the shaft around O_{i3} from the offset static. Thus, the angle between vector $\boldsymbol{r}_{O_{i2}^{'}O_{i3}}$ and axis $z_j^{'}$ can be calculated as follows:

$$\theta_z^{'}=\theta_z+\Delta\theta. \tag{13}$$

From the geometric relationship, points O^P and O^R are on the vectors $\boldsymbol{r}_{O_{i2}O_{i3}}$ and $\boldsymbol{r}_{O_{i2}^{'}O_{i3}}$, respectively. Thus, the vector from O^P to O^R can be determined as follows:

$$\boldsymbol{r}_{O^PO^R}=\begin{bmatrix} \left\|\boldsymbol{r}_{O^PO_{i3}}\right\|\sin\theta_z-\left\|\boldsymbol{r}_{O^RO_{i3}}\right\|\sin\theta_z^{'} \\ 0 \\ \left\|\boldsymbol{r}_{O^PO_{i3}}\right\|\cos\theta_z-\left\|\boldsymbol{r}_{O^RO_{i3}}\right\|\cos\theta_z^{'} \end{bmatrix}. \tag{14}$$

Given that the distance from the center of shaft to the center of the inner raceway is a constant value, Eq. (14) can be simplified into

$$\boldsymbol{r}_{O^PO^R}=\left\|\boldsymbol{r}_{O^PO_{i3}}\right\|\left[\sin\theta_z-\sin\theta_z^{'},\ 0,\ \cos\theta_z-\cos\theta_z^{'}\right]^T. \tag{15}$$

Thus, the position vector of the shaft center O^R can be obtained from Eq. (16) as

$$\boldsymbol{r}_{O^R}=\boldsymbol{r}_{O^P}+\boldsymbol{r}_{O^PO^R}. \tag{16}$$

Overall, shaft poses in the deflection static can be determined by $\boldsymbol{r}_{O^R}$ and the angle deflection $\Delta\theta$.

In the 3D space, any center plane of the two outer rings can be taken as the fixed reference plane and the reference frame $O_j^{'}-x_j^{'}y_j^{'}z_j^{'}$ on it as the fixed reference frame $O_j-x_jy_jz_j$, as shown in Fig. 5. Thus, the reference frame $O_j^{'}-x_j^{'}y_j^{'}z_j^{'}$ on the

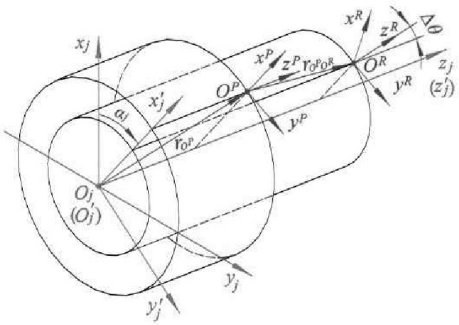

Fig. 5. Relative poses between the shaft and outer rings in 3D space.

rest of the center plane of the two outer rings can be obtained by rotating reference frame $O_j - x_j y_j z_j$ around its axis z_j with an angle of α_j.

Therefore, the static pose of the shaft relative to the outer rings can be determined by the pose description of $O_{vj} - x_{vj} y_{vj} z_{vj}$ relative to $O_j - x_j y_j z_j$. According to homogeneous coordinate transformation theory, the static pose of the shaft can be described as

$$ {}^{j}\boldsymbol{T}_{vj} = \begin{cases} {}^{j}\boldsymbol{T}_{P} : \boldsymbol{Rot}\left(z,\alpha_j\right)\boldsymbol{Trans}\left(\boldsymbol{r}_{O^P}\right), \text{ Offset static} \\ {}^{j}\boldsymbol{T}_{R} : \boldsymbol{Rot}\left(z,\alpha_j\right)\boldsymbol{Trans}\left(\boldsymbol{r}_{O^R}\right)\boldsymbol{Rot}\left(y,\Delta\theta\right), \text{ Deflection static} \end{cases}, \tag{17} $$

where ${}^{j}\boldsymbol{T}_{i}$ denotes the homogeneous transformation matrix from $O_j - x_j y_j z_j$ to $O_i - x_i y_i z_i$, and ***Rot*** and ***Trans*** denote the rotation and translation operators [53], respectively.

From Eq. (17), as long as all solutions that are determined by α_j and $r_{O^P}^{x}$ are obtained, the static deviation law of the PBS-joint shaft considering the clearance in 3D space can be completely determined. Figs. 6 and 7 show the deviation laws of offset static and deflection static by substituting the parameters of joint 1 presented in Table 2. The outline of the central area is the center trajectory of the shaft corresponding to $G_r = 2\ \mu m$. The outer boundary corresponds to $G_r = 13\ \mu m$. Therefore, when G_r is taken in the range of 2-13 μm, the center of the PBS-joint shaft inevitably falls into the closed space constituted by the outline of the central area and the outer boundary shown in Figs. 6 and 7, which is the error space of joint 1.

According to deviation laws, the PBS-joint shaft is allowed to have great displacement along the axial direction under offset static state. When $G_r = 2\ \mu m$ and $G_r = 13\ \mu m$, the ranges of axial displacement are 13 and 5 times of G_r, respectively. Under the deflection static state, the shaft is allowed to rotate with maximum angles of 4.16×10^{-4} rad and 6.44×10^{-5} rad, respectively. However, the allowed displacement of the shaft center is very small. Apparently, these deviations significantly affect the accuracy of the mechanism. However, when the plane-joint clearance model is used to analyze the influence of PBS-joint clearance on the mechanism accuracy, all the above situations cannot be considered. Therefore, the PBS-joint clearance model proposed in this work has the capacity to

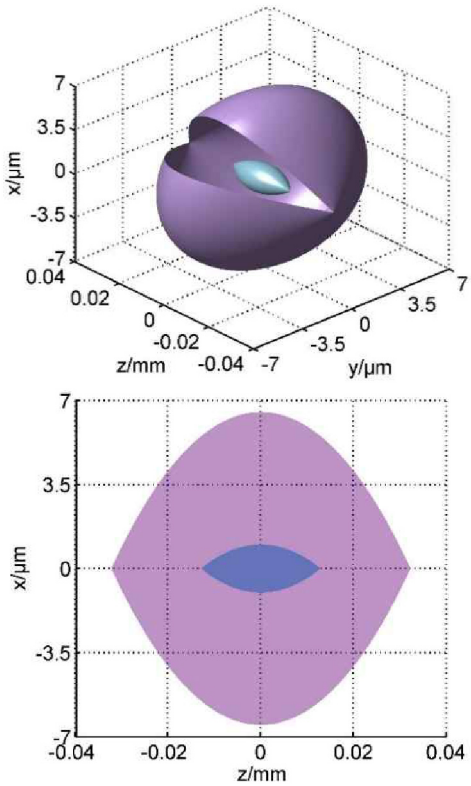

Fig. 6. Error space of PBS-joint in offset static.

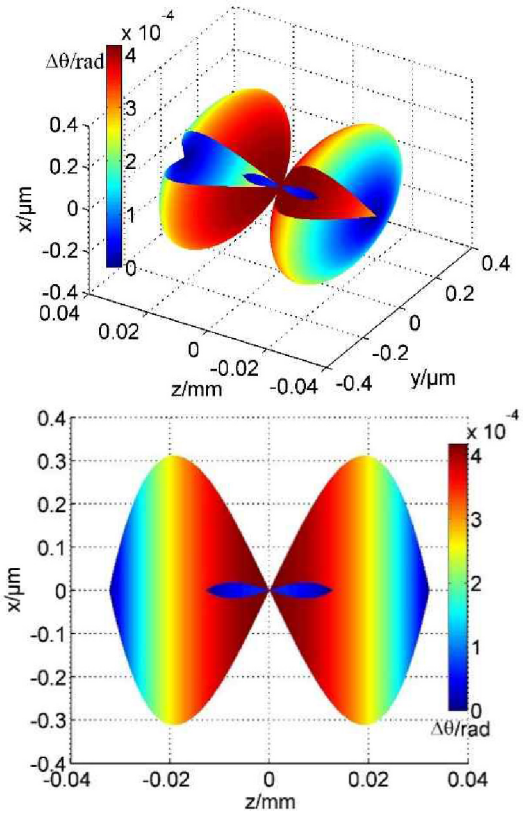

Fig. 7. Error space of PBS-joint in deflection static.

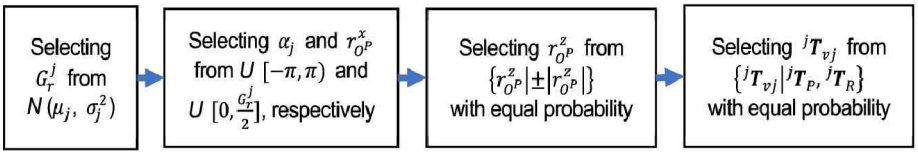

Fig. 8. Selection process of deviation static type of PBS-joint.

achieve enhanced analysis mechanism accuracy.

2.2 Selection of deviation static type

The bearing radial clearance G_r is generated from the errors of bearing machining and installation and is a random variable subject to normal distribution. According to 3σ principles, the values of G_r are almost all concentrated in the interval $(\mu-3\sigma, \mu+3\sigma)$. Therefore, for G_r^j, the bearing radial clearance on the j-th joint, its mean value μ_j, and standard deviation σ_j can be determined by Eq. (18):

$$\begin{cases} \mu_j = \dfrac{\max\left(G_r^j\right)+\min\left(G_r^j\right)}{2} \\ \sigma_j = \dfrac{\max\left(G_r^j\right)-\mu_j}{3} \end{cases}, \tag{18}$$

where $\max\left(G_r^j\right)$ and $\min\left(G_r^j\right)$ respectively denote the upper and lower limits of j-th joint radial clearance. Note that according to the assumptions in Sec. 2.1, the clearances of two bearings in the same joint are equal.

Assuming that the force or torque acting on the joint is uniform and random, the joint has no external constraints. Thus, the azimuth angle α_j is consistent with the uniform random distribution in $[-\pi,\pi)$, and the radial offset displacement $r_{O^P}^x$ is consistent with the uniform random distribution in $\left[0,\dfrac{G_r^j}{2}\right]$.

According to Eq. (3), for any determined α_j and $r_{O^P}^x$, there are two offset static states between the shaft and outer rings. Every offset static state can also determine one deflection static state. As a result, the PBS-joint has four possible static states that correspond to one determined α_j and $r_{O^P}^x$, and the selection process of the final static state is uniform and random. Fig. 8 shows the selection process of deviation static type.

3. Deviation transmission model

3.1 Deviation transmission model of serial mechanism

Denavit-Hartenberg (D-H) method [54] can be easily used to describe the pose relationships between links. This method stipulates the law of homogeneous transformation from reference frame $O_j - x_j y_j z_j$ to $O_{j+1} - x_{j+1} y_{j+1} z_{j+1}$ as follows,

$$\begin{aligned} {}^jT_{j+1} &= \boldsymbol{Rot}\left(z,\theta_{j+1}\right)\boldsymbol{Trans}\left(0,0,d_{j+1}\right)\boldsymbol{Trans}\left(l_{j+1},0,0\right)\boldsymbol{Rot}\left(x,\beta_{j+1}\right), \\ &= \begin{bmatrix} {}^jR_{j+1} & {}^jP_{j+1} \\ 0 & 1 \end{bmatrix}, \end{aligned} \tag{19}$$

where

$${}^jR_{j+1} = \begin{bmatrix} \cos\theta_{j+1} & -\sin\theta_{j+1}\cos\beta_{j+1} & \sin\theta_{j+1}\sin\beta_{j+1} \\ \sin\theta_{j+1} & \cos\theta_{j+1}\cos\beta_{j+1} & -\cos\theta_{j+1}\sin\beta_{j+1} \\ 0 & \sin\beta_{j+1} & \cos\beta_{j+1} \end{bmatrix},$$

$${}^jP_{j+1} = \begin{bmatrix} l_{j+1}\cos\theta_{j+1} \\ l_{j+1}\sin\theta_{j+1} \\ d_{j+1} \end{bmatrix}, \quad \theta_{j+1} \text{ is the rotation angle from } x_j \text{ to } x_{j+1} \text{ around } z_j, \quad d_{j+1} \text{ is the perpendicular distance from } x_j \text{ to } x_{j+1} \text{ along } z_j, \quad l_{j+1} \text{ is the perpendicular distance from } z_j \text{ to } z_{j+1} \text{ along } x_{j+1}, \text{ and } \beta_{j+1} \text{ is the rotation angle from } z_j \text{ to } z_{j+1} \text{ around } x_{j+1}.$$

The establishment of the moving reference frame $O_{j+1} - x_{j+1} y_{j+1} z_{j+1}$ on joint $j+1$ needs to be consistent with the following laws, as shown in Fig. 9.

(1) The origin of the reference frame is fixed at the intersection of the common normal of two adjacent joint axes and the axis of joint $j+1$.

(2) The coefficient x_{j+1} coincides with the common normal, and the direction is from joint j to joint $j+1$.

(3) The coefficient z_{j+1} is collinear with the axis of joint $j+1$.

(4) The coefficient y_{j+1} is determined by the right-hand law.

To establish the moving reference frame on each joint of the mechanism according to the above laws, the pose of link $j+1$ described in fixed reference frame $O-XYZ$ can be determined as

$${}^0T_{j+1} = \prod_{i=0}^{j} T_{i+1}. \tag{20}$$

As shown in Fig. 1, when the shaft of the PBS-joint deviates from the designed state, the two links connected by the joint will deviate correspondingly. The spatial virtual link vj is used to describe the deviation. A virtual joint vj is introduced to connect link vj and link $j+1$. When joint clearance is taken into consideration, the links connected by the PBS-joint can be equivalent to a model shown in Fig. 10, where the pose of reference frame $O_{vj} - x_{vj} y_{vj} z_{vj}$ described in $O_j - x_j y_j z_j$ can be

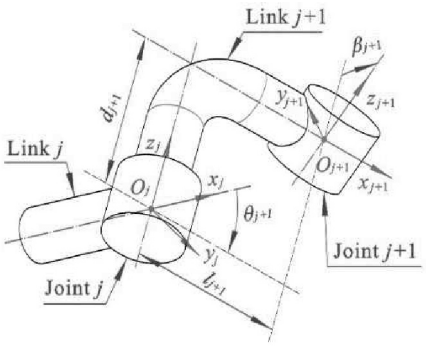

Fig. 9. Relative pose of adjacent links.

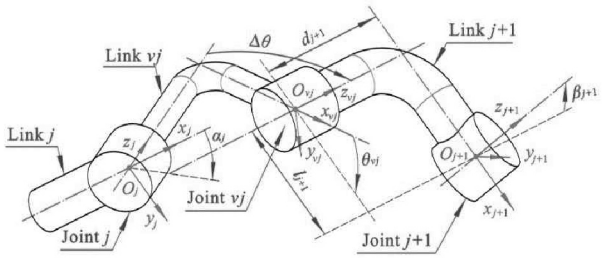

Fig. 10. Equivalent model of adjacent links with PBS-joint clearance considered.

obtained by Eq. (17). The link $j+1$ is fixed with the shaft. Thus, the link and the shaft have the same deviation. When the shaft has no rotation displacement relative to its axis, the angle from plane $O_j - x_j z_j$ to the plane formed by axes z_j and x_{j+1} in Fig. 10 is the similar to the angle in Fig. 9, both are θ_{j+1}. Given that the angle from plane $O_j - x_j z_j$ to plane $O_{vj} - x_{vj} z_{vj}$ is α_j, the angle from plane $O_{vj} - x_{vj} z_{vj}$ to the plane formed by axes z_{vj} and x_{j+1} can be obtained by

$$\theta_{vj} = \theta_{j+1} - \alpha_j . \tag{21}$$

The obtained θ_{vj} is the angle from x_{vj} to x_{j+1} around z_{vj}.

According to the definition of each parameter in Eq. (19), for the links connected by revolute joint, parameters d_{j+1}, l_{j+1} and β_{j+1} are all fixed values in the process of motion. Therefore, the homogeneous transformation matrix from link vj to link $j+1$ is

$${}^{vj}\boldsymbol{T}_{j+1} = {}^{j}\boldsymbol{T}_{j+1}\left(\theta_{vj}, d_{j+1}, l_{j+1}, \beta_{j+1}\right). \tag{22}$$

The homogeneous transformation matrix from link j to link $j+1$ with PBS-joint shaft deviated can then be obtained from Eq. (23) as follows:

$${}^{j}\boldsymbol{A}_{j+1} = {}^{j}\boldsymbol{T}_{vj}\,{}^{vj}\boldsymbol{T}_{j+1} . \tag{23}$$

According to the homogeneous transformation law, when only PBS-joint clearances are considered, the pose of link $j+1$ described in the fixed reference frame $O-XYZ$ can be obtained by Eq. (24):

$${}^{0}\boldsymbol{A}_{j+1} = \prod_{i=0}^{j} \boldsymbol{A}_{i+1} . \tag{24}$$

To distinguish the differences between $O_{j+1} - x_{j+1} y_{j+1} z_{j+1}$ in the ideal state (Fig. 9) and the state of considering the PBS-joint clearance (Fig. 10), $O_{c(j+1)} - x_{c(j+1)} y_{c(j+1)} z_{c(j+1)}$ is used to denote the $O_{j+1} - x_{j+1} y_{j+1} z_{j+1}$ in the state of considering the PBS-joint clearance. Then, the deviation of link $j+1$ caused by the PBS-joint clearance can be obtained by Eq. (25):

$${}^{j+1}\boldsymbol{T}_{c(j+1)} = {}^{0}\boldsymbol{T}_{j+1}^{-1}\,{}^{0}\boldsymbol{A}_{j+1} = \begin{bmatrix} {}^{j+1}\boldsymbol{R}_{c(j+1)} & {}^{j+1}\boldsymbol{P}_{c(j+1)} \\ 0 & 1 \end{bmatrix}, \tag{25}$$

where ${}^{j+1}\boldsymbol{R}_{c(j+1)}$ and ${}^{j+1}\boldsymbol{P}_{c(j+1)}$ are the attitude and position deviations described in $O_{j+1} - x_{j+1} y_{j+1} z_{j+1}$.

To intuitively reflect the deviation of link $j+1$, the position deviation $\boldsymbol{P}_{j+1}^{e}$ described in the fixed reference frame $O-XYZ$ is used to show the position deviation that can obtained by Eq. (26). The Euler angle is used to represent the attitude deviation. According to the relationship between rotation matrix and Euler angle shown in Eq. (27), the attitude deviation $\boldsymbol{\varphi}_{j+1}^{e}$ can be determined as shown in Eq. (28):

$$\boldsymbol{P}_{j+1}^{e} = {}^{o}\boldsymbol{P}_{c(j+1)} - {}^{o}\boldsymbol{P}_{j+1} , \tag{26}$$

where ${}^{o}\boldsymbol{P}_{j+1}$ and ${}^{o}\boldsymbol{P}_{c(j+1)}$ are determined by Eqs. (20) and (24), respectively.

$$\boldsymbol{R}_{Euler} = \boldsymbol{Rot}\left(z,\theta_z\right)\boldsymbol{Rot}\left(y,\theta_y\right)\boldsymbol{Rot}\left(x,\theta_x\right), \tag{27}$$

$$\boldsymbol{\varphi}_{j+1}^{e} = \left[\theta_x, \theta_y, \theta_z\right]^{T} , \tag{28}$$

where

$\theta_x = \operatorname{atan2}\left({}^{j+1}\boldsymbol{R}_{c(j+1)}(3,2), {}^{j+1}\boldsymbol{R}_{c(j+1)}(3,3)\right)$;

$\theta_y = \operatorname{atan2}\left(-{}^{j+1}\boldsymbol{R}_{c(j+1)}(3,1), \sqrt{{}^{j+1}\boldsymbol{R}_{c(j+1)}^{2}(3,2) + {}^{j+1}\boldsymbol{R}_{c(j+1)}^{2}(3,3)}\right)$;

$\theta_z = \operatorname{atan2}\left({}^{j+1}\boldsymbol{R}_{c(j+1)}(2,1), {}^{j+1}\boldsymbol{R}_{c(j+1)}(1,1)\right)$; and

${}^{j+1}\boldsymbol{R}_{c(j+1)}(i,j)$ denotes the row i column j element of ${}^{j+1}\boldsymbol{R}_{c(j+1)}$.

$$a\tan 2(y,x) = \begin{cases} \arctan\left(\dfrac{y}{x}\right); & x > 0 \\ \arctan\left(\dfrac{y}{x}\right) + \pi; & y \geq 0,\ x < 0 \\ \arctan\left(\dfrac{y}{x}\right) - \pi; & y < 0,\ x < 0 \\ \dfrac{\pi}{2}; & y > 0,\ x = 0 \\ -\dfrac{\pi}{2}; & y < 0,\ x = 0 \\ undefined; & y = 0,\ x = 0 \end{cases} .$$

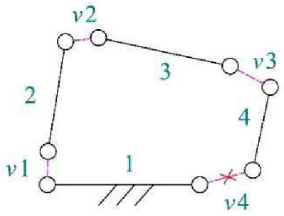

Fig. 11. Equivalent model of single-loop mechanism with joint clearances.

In the serial mechanism, the states of clearance joints can be considered independent of each other. The deviations are transmitted step by step from the starting link to the end link. Therefore, the parameters of ${}^{j}\boldsymbol{T}_{vj}$ in Eq. (23) only need to follow the selection laws in Fig. 8, and the deviation of each link can be directly determined by Eqs. (26) and (28).

3.2 Deviation transmission model of multi-loop mechanism

Different from the serial mechanism, the links in the multi-loop mechanism forms a number of single-loop structures. The pose of each link after deviation must meet the geometric closure condition. Thus, every joint state in the multi-loop mechanism is coupled to each other. The determination of the geometric closure condition of the deviated mechanism and the establishment of the coupling relationship between each link and joint are the keys to analyzing the error of the multi-loop mechanism.

Any single-loop mechanism with joint clearance can be equivalent to the model shown in Fig. 11 by adopting the spatial virtual link vj. When one of the virtual links is removed from the frame, such as the virtual link $v4$, the equivalent model will be transformed into a serial mechanism. According to Eq. (23), the pose of the obtained serial mechanism can be easily solved. Meanwhile, regardless of what pose the obtained serial mechanism is in, the mechanism still needs to be able to form a geometrically closed loop with the frame and virtual link $v4$. Therefore, the attitude and end position of the link (link 4) connected with the removed virtual link (virtual link $v4$) must be in the error space of the joint whose clearance is equivalent to the removed virtual link. On the basis of Eqs. (26) and (28), the pose error space of each link in the single-loop mechanism can be described as

$$\boldsymbol{\Gamma}_s = \left\{ \boldsymbol{P}^e_{j+1}, \boldsymbol{\varphi}^e_{j+1} | \boldsymbol{P}^e_n, \boldsymbol{\varphi}^e_n \in \boldsymbol{\Theta}_n, 1 \le j \le n-1 \right\}, \tag{29}$$

where n is the number of links in the single-loop mechanism, and $\boldsymbol{\Theta}_n$ is the error space of the n-th joint determined by Eq. (17).

Similar to the serial mechanism or single-loop mechanism, which uses link as the carrier of deviation transmission, for the multi-loop mechanism, the single loop can be used as the carrier. Ref. [49] pointed out that in the multi-loop mechanism, the transmission of deviation is similar to the spread of water waves. The deviation transmission laws were based on the low-layer loop sequence description method of the topological structure relations listed as follows:

(1) The deviation is transmitted from the single loop in the lower rank to the single loop in the higher rank.

(2) Among single loops in the same rank, the deviation is transmitted from the loop in low assembly sequence to the loop in high assembly sequence.

(3) If the loop belongs to the coupled loop set, the deviation is directly transmitted from other loops to the coupled loop set containing the loop.

(4) The frame of the single loop is the shared link between adjacent single loops that are in low rank or low assembly sequence.

Therefore, to analyze the deviation law of the multi-loop mechanism, the rank and assembly sequence of each single loop need to be determined first. Ref. [49] used the distance from the single loop to the frame as the rank division standard. However, the definition and calculation method of the distance were not presented. To make the method more formal, the rank calculation formula shown in Eq. (30) is used to determine the rank of single loops in a multi-loop mechanism:

$$lll(M) = N + 1, \tag{30}$$

where M denotes the mark number of the single loop in the multi-loop mechanism, $lll(M)$ denotes the rank of single loop M, and N denotes the minimum number of single loops from the frame to single loop M that should be passed (i.e., the distance from frame to single loop M).

The assembly sequence of the single loops in the same rank is defined as follows. If a parent-child assembly relationship exists between the single loops, then sort them through this relationship from inside to outside. If the parallel relationship exists, then sort them by clockwise or anti-clockwise sequence. The coupled loop set is the set of all single loops sharing the same public link. The public link referred to here is the link that participates in two or more single-loop configurations, with each single loop containing only a portion of the link.

According to the above deviation transmission laws, the frame of each single loop in the multi-loop mechanism can be defined and the geometric closure conditions can be determined. Thus, from Eq. (29), the error space of each single loop can be obtained. The obtained error spaces are the error space of the multi-loop mechanism. Thus, the accuracy analysis of the multi-loop mechanism needs to start from the first assembly sequence single loop located in the lowest rank to calculate the error space of each single loop step by step. To obtain the unified error space expression of the multi-loop mechanism, the single-loop mark number M can be defined as

$$M = \left[lll(M) - 1 \right] N_{lll(M)} + K_M. \tag{31}$$

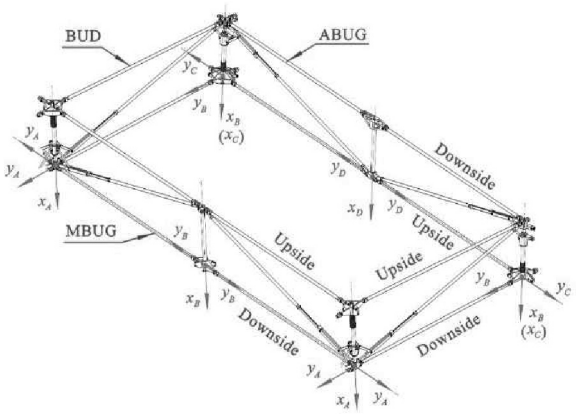

Fig. 12. Basic loop mechanism.

where $N_{III(M)}$ is the number of single loops in rank $III(M)$, and K_M is the assembly sequence number of single loop M.

Therefore, the error space of the multi-loop mechanism can be uniformly described as

$$\mathbf{\Gamma}_m = \left\{ \mathbf{\Gamma}_s^M | 1 \le M \le \max(M) \right\}, \tag{32}$$

where $\mathbf{\Gamma}_s^M$ is the error space of single loop M determined by Eq. (29).

4. Case analysis

4.1 Mechanism configuration

The basic loop mechanism of a space-borne parabolic antenna is subjected to a case analysis (Fig. 12). The basic loop mechanism is composed of three basic units: The basic unit on the directrix (BUD), the main basic unit on the generatrix (MBUG), and the assistant basic unit on the generatrix (ABUG). The upside and downside of MBUG and ABUG are opposite and parallel to one another. The MBUG and BUD are vertical and share the same slider. The configurations of these three basic units are the same with different scales, as shown in Fig. 13. The working principle is as follows: the spring pushes slider $3'$ to move along the axis $f'k'$ and drives each link to move until the link de' touches the mechanical limit point H, where the link de' and cd are collinear. Therefore, the mechanism gets self-locked in the deployed state.

According to the task requirements, the antenna reflector is installed on the downside of BUD and MBUG (fixed at points A and B) and the upside of ABUG (fixed at points C and D). Therefore, points A and B of BUD and MBUG and points C and D of ABUG are the key factors to determine the geometric characteristics of the antenna. These factors are taken as reference points in the accuracy analysis of the basic loop mechanism in practical engineering.

To analyze the accuracy of the basic loop mechanism, the reference frames as shown in Fig. 13 are established at points A and B of BUD and MBUG and C and D of ABUG. The axis x of each reference frame coincides with link AC or link BD,

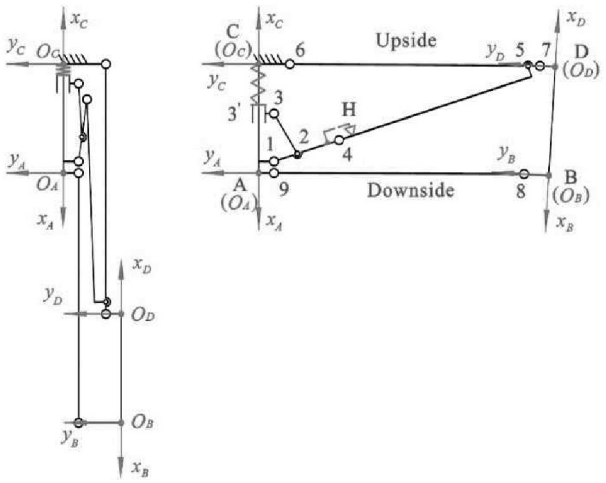

(a) Folded state (b) Deployed state

Fig. 13. Schematic of basic unit.

and its direction points to the side where the reflector is fixed. The direction of axis y is shown in Fig. 13, and the direction of axis z is determined by the right-hand law. The spatial distribution of each reference frame is shown in Fig. 12, where the axis z is omitted.

4.2 Deviation calculation model

The link AC is a public link that participates in the construction of all single loops in the same basic unit. Thus, the single loops form a coupled-loop set. According to the deviation transmission laws of the multi-loop mechanism, the deviation of each single loop in the basic loop mechanism will be directly transmitted to the adjacent basic unit. Therefore, the accuracy analysis of the basic loop mechanism can be divided into two parts: (1) Addressing the deviation transmission laws in the basic unit and (2) addressing the deviation transmission laws between basic units.

(1) Deviation transmission laws in the basic unit

The basic loop mechanism is in a self-locked state after being deployed. In microgravity, the forces on the mechanism can be ignored except the force from the spring. In the deployed state, the spring only provides a small force for self-locking, and the deformation of each component can be ignored. Thus, the mechanism can be regarded as a multi-rigid body system.

The basic unit consists of one slide joint and nine revolute joints. The revolute joints are all PBS-joints, and the slide joint is realized by precision linear bearing, where the clearance can be ignored. Therefore, the basic unit can be regarded as a mechanism that only contains PBS-joint clearances. The basic loop mechanism is self-locked and the components are statistically balanced when deployed. Thus, the deviation laws of the joint shaft can be determined by Eq. (17), and the selection of the static type also follows the process shown in Fig. 8.

Three single loops are present in the basic unit (Fig. 14).

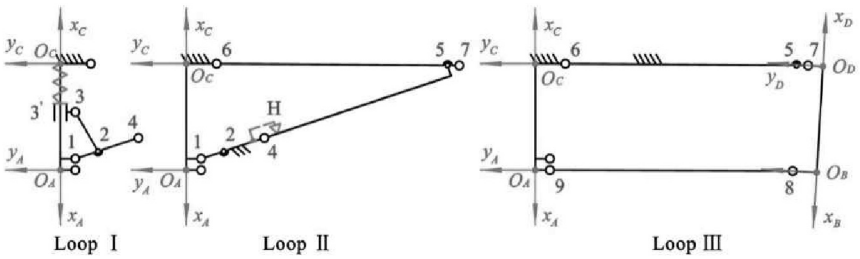

Fig. 14. Single loops in basic unit.

From Eq. (30), when the link AC is selected as the frame, these three single-loops are in the same rank and, according to the parent-child assembly relationship, the assembly sequence of loops I-III corresponds to 1-3, respectively. Therefore, the analysis needs to start from loop I.

The reference frame $O_A - x_A y_A z_A$ is taken as the fixed reference frame of BUD and MBUG. The reference frame $O_C - x_C y_C z_C$ is taken as the fixed reference frame of ABUG. The moving reference frame $O_j - x_j y_j z_j$ is set at revolute joint j according to the D-H method, where, the z_j axis direction is followed the Z axis direction of the fixed reference frame. Therefore, the z axis direction of each reference frame in BUD and MBUG is opposite to the reference frames in ABUG.

For BUD and MBUG, the frame of loop I is link AC. According to the deviation transmission law of single loop, the homogeneous transformation matrix from the fixed reference frame to joint 4 can be obtained from Eq. (33), where ${}^{A}\boldsymbol{T}_4$ and ${}^{A}\boldsymbol{A}_4$ are the matrix obtained under the ideal condition and the condition of taking the joint clearance into consideration, respectively.

$$\begin{cases} {}^{A}\boldsymbol{T}_4 = {}^{A}\boldsymbol{T}_1\,{}^{1}\boldsymbol{T}_4 \\ {}^{A}\boldsymbol{A}_4 = {}^{A}\boldsymbol{A}_1\,{}^{1}\boldsymbol{A}_4 \\ s.t.\ \boldsymbol{P}_3^e, \boldsymbol{\varphi}_3^e \in \boldsymbol{\Theta}_3 \end{cases}. \tag{33}$$

The frame of loop II is the shared link with loop I (i.e., the link AC and link 14). Hence, the homogeneous transformation matrix from the fixed reference frame to joint 7 can be obtained from Eq. (34) as follows:

$$\begin{cases} {}^{A}\boldsymbol{T}_7 = {}^{A}\boldsymbol{T}_4\,{}^{4}\boldsymbol{T}_5\,{}^{5}\boldsymbol{T}_6\,{}^{6}\boldsymbol{T}_7 \\ {}^{A}\boldsymbol{A}_7 = {}^{A}\boldsymbol{A}_4\,{}^{4}\boldsymbol{A}_5\,{}^{5}\boldsymbol{A}_6\,{}^{6}\boldsymbol{T}_7 \\ s.t.\ \boldsymbol{P}_6^e, \boldsymbol{\varphi}_6^e \in \boldsymbol{\Theta}_6 \end{cases}. \tag{34}$$

The frame of loop III is the shared link with loop II (i.e., the link AC and link 67). Thus, the homogeneous transformation matrix from the fixed reference frame to point B can be obtained from Eq. (35) as follows:

$$\begin{cases} {}^{A}\boldsymbol{T}_B = {}^{A}\boldsymbol{T}_7\,{}^{7}\boldsymbol{T}_D\,{}^{D}\boldsymbol{T}_B \\ {}^{A}\boldsymbol{A}_B = {}^{A}\boldsymbol{A}_7\,{}^{7}\boldsymbol{A}_D\,{}^{D}\boldsymbol{A}_B \\ s.t.\ \boldsymbol{P}_9^e, \boldsymbol{\varphi}_9^e \in \boldsymbol{\Theta}_9 \end{cases}. \tag{35}$$

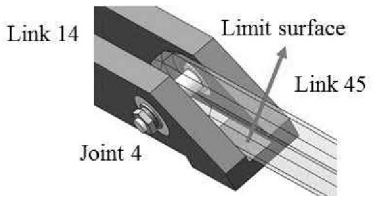

Fig. 15. Mechanical limiting structure at joint 4.

Similarly, in ABUG, according to the relationships between moving reference frame and $O_C - x_C y_C z_C$, the homogeneous transformation matrix from the fixed reference frame $O_C - x_C y_C z_C$ to point D can be obtained, as denoted by ${}^{C}\boldsymbol{T}_D$ and ${}^{C}\boldsymbol{A}_D$. The parameters in ${}^{A}\boldsymbol{T}_B$, ${}^{A}\boldsymbol{A}_B$, ${}^{C}\boldsymbol{T}_D$, and ${}^{C}\boldsymbol{A}_D$ are substituted into Eqs. (25), (26) and (28). Then, the deviation of the basic unit can be obtained.

The deployment ending position of the basic unit is determined by the mechanical limiting point H. link 45 will always be in contact with point H in the deployed state. When the clearance exists in joint 4, the relative pose between link 45 and link 14 may deviate from the design state. According to the mechanism-limiting structure (Fig. 15), the projection point of point H on the axis of joint 4 is located between the two support bearings, and the limit surface is always perpendicular to the plane $O_4 - x_4 y_4$. Therefore, when the constraints introduced by factors such as friction and deformation, among others, are considered, the support reaction of point H to link 45 must be parallel to the plane $O_4 - x_4 y_4$ and is located between the two support bearings. According to the force-balance principle of the rigid body, the direction of support reaction provided by the outer ring of two support bearings must be the same. Thus, the joint shaft cannot be deflected, and joint 4 should only be in the offset static. In addition, because link 45 should still be in contact with point H after deviation, as shown in Fig. 16, the joint shaft will rotate around its own axis, which will make link 45 rotate an angle of θ_H around z_4. According to the sine theorem, the following relationship can be obtained:

$$\frac{\sin\left[\pi - \theta_H + |\alpha_4|\right]}{\left|\boldsymbol{r}_{O_4 H}\right|} = \frac{\sin\theta_H}{r_{O^P}^{x}}. \tag{36}$$

From Eq. (36), θ_H can be solved and described as

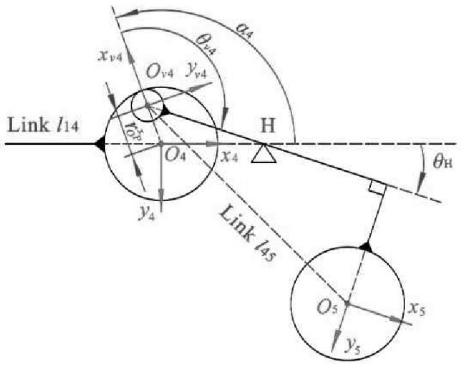

Fig. 16. Clearance model of joint 4 (ABUG).

$$\theta_H = \arctan\left(\frac{r_{O^P}^x \sin|\alpha_4|}{|\boldsymbol{r}_{O_4H}| - r_{O^P}^x \cos|\alpha_4|}\right); \theta_H \in \left[0, \frac{\pi}{2}\right). \tag{37}$$

The z direction of the reference frames in BUD and MBUG is opposite to the reference frames in ABUG. Thus, when corresponding to the different basic unit, the value of parameter θ_{v4} in Eq. (34) is different and can be obtained by Eq. (38).

$$\theta_{v4} = \begin{cases} \theta_H - \alpha_4;\ \alpha_4 \in [-\pi, 0],\ ABUG \\ -\theta_H - \alpha_4;\ \alpha_4 \in [0, \pi],\ BUD \text{ and } MBUG \end{cases} \tag{38}$$

(2) Deviation transmission law between basic units

The relative pose error between $O_A - x_A y_A z_A$ and $O_B - x_B y_B z_B$ characterizes the deviations of BUD and MBUG, and the relative pose error between $O_C - x_C y_C z_C$ and $O_D - x_D y_D z_D$ characterizes the deviations of ABUG. Therefore, the above reference frames can be regarded as the characteristic reference frames (CRFs) of the basic unit. The relations between CRFs can be equivalent to a characteristic link. From the characteristic link, the deviation characteristics of the basic unit can be obtained. The relations between basic units can be easily described.

The equivalent model of the basic loop mechanism described by characteristic links is shown in Fig. 17, where L_{AB}^D, L_{AB}^M, and L_{CD}^A denote the characteristic links of BUD, MBUG, and ABUG, respectively. According to the structural characteristics shown in Fig. 12, when the link AC at point I in the equivalent model is selected as the frame of the basic loop mechanism, the single loops will be assigned into three ranks. Among these single loops, those in the basic units containing point IV will be assigned into the highest rank. The deviation of each basic unit will be transmitted by two paths to point IV (i.e., by I-II-III-IV and I-VI-V-IV).

The CRFs at the beginning of each characteristic link defined clockwise as the pose characterization reference frame (PCRF) $O_i - x_i y_i z_i$ ($i = \mathrm{I} - \mathrm{VI}$) of each point is used to uniquely describe the state of each point, as shown in Fig. 17(b). According to the structural characteristics of the basic loop mechanism, the homogeneous transformation matrix between adjacent PCRFs can be directly determined from Table 1.

Table 1. Homogeneous transformation matrix between each PCRF*.

Index	Ideal state	Deviated state
$\boldsymbol{B}(\mathrm{II})$	${}^{\mathrm{I}}\boldsymbol{T}_{\mathrm{II}} = {}_M^A\boldsymbol{T}_B \boldsymbol{Rot}(x, \pi)$	${}^{\mathrm{I}}\boldsymbol{A}_{\mathrm{II}} = {}_M^A\boldsymbol{A}_B \boldsymbol{Rot}(x, \pi)$
$\boldsymbol{B}(\mathrm{III})$	${}^{\mathrm{II}}\boldsymbol{T}_{\mathrm{III}} = {}_M^A\boldsymbol{T}_B^{-1} \boldsymbol{Rot}\left(x, -\frac{\pi}{2}\right)$	${}^{\mathrm{II}}\boldsymbol{A}_{\mathrm{III}} = {}_M^A\boldsymbol{A}_B^{-1} \boldsymbol{Rot}\left(x, -\frac{\pi}{2}\right)$
$\boldsymbol{B}(\mathrm{IV})$	${}^{\mathrm{I}}\boldsymbol{T}_{\mathrm{VI}} = \boldsymbol{Rot}\left(x, \frac{\pi}{2}\right) {}_D^A\boldsymbol{T}_B$	${}^{\mathrm{I}}\boldsymbol{A}_{\mathrm{VI}} = \boldsymbol{Rot}\left(x, \frac{\pi}{2}\right) {}_D^A\boldsymbol{A}_B$
$\boldsymbol{B}(\mathrm{V})$	${}^{\mathrm{VI}}\boldsymbol{T}_{\mathrm{V}} = \boldsymbol{Rot}\left(x, -\frac{\pi}{2}\right) {}_A^C\boldsymbol{T}_D$	${}^{\mathrm{VI}}\boldsymbol{A}_{\mathrm{V}} = \boldsymbol{Rot}\left(x, -\frac{\pi}{2}\right) {}_A^C\boldsymbol{A}_D$
$\boldsymbol{B}(\mathrm{VI})$	${}^{\mathrm{V}}\boldsymbol{T}_{\mathrm{IV}} = \boldsymbol{Rot}(x, \pi) {}_A^C\boldsymbol{T}_D^{-1}$	${}^{\mathrm{V}}\boldsymbol{A}_{\mathrm{IV}} = \boldsymbol{Rot}(x, \pi) {}_A^C\boldsymbol{A}_D^{-1}$

*: In Table 1, ${}_k^i\boldsymbol{T}_j$ and ${}_k^i\boldsymbol{A}_j$ denote ${}^i\boldsymbol{T}_j$ and ${}^i\boldsymbol{A}_j$, which are calculated by substituting the geometrical parameters of basic unit k, where $k = D, M, A$ represent BUD, MBUG, and ABUG, respectively.

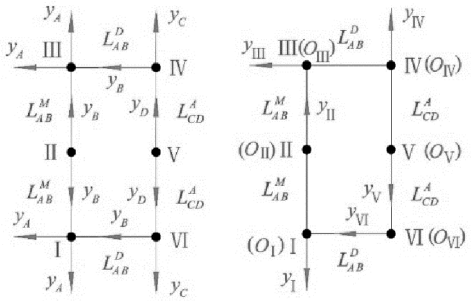

(a) Distribution of CRFs (b) Distribution of PCRFs

Fig. 17. Equivalent model of basic loop mechanism.

According to the deviation transmission path, the homogeneous transformation matrix from the PCRF at point I to the rest PCRFs can be obtained by

$${}^{\mathrm{I}}\boldsymbol{T}_i \text{ or } {}^{\mathrm{I}}\boldsymbol{A}_i = \begin{cases} \prod_{j=\mathrm{II}}^{i} \boldsymbol{B}(j);\ i = \mathrm{II}, \mathrm{III} \\ \prod_{j=\mathrm{IV}}^{\mathrm{X}-i} \boldsymbol{B}(j);\ i = \mathrm{IV}, \mathrm{V}, \mathrm{VI}, \\ s.t.\ \boldsymbol{P}_{\mathrm{IV}}^e, \boldsymbol{\varphi}_{\mathrm{IV}}^e \in \boldsymbol{\Theta}_{L_{AB}^D} \end{cases} \tag{39}$$

where ${}^{\mathrm{I}}\boldsymbol{T}_i$ and ${}^{\mathrm{I}}\boldsymbol{A}_i$ denote the homogeneous transformation matrix calculated by substituting the corresponding elements in the ideal state column and deviated state column into $\boldsymbol{B}(j)$, respectively. $\boldsymbol{P}_{\mathrm{IV}}^e$ is obtained by Eq. (40) directly, $\boldsymbol{\varphi}_{\mathrm{IV}}^e$ is obtained by substituting ${}^B\boldsymbol{R}_{\mathrm{IV}}$ in Eq. (40) into Eq. (28). $\boldsymbol{\Theta}_{L_{AB}^D}$ denote the error space of the characteristic link L_{AB}^D.

$$\begin{bmatrix} {}^B\boldsymbol{R}_{\mathrm{IV}} & \boldsymbol{P}_{\mathrm{IV}}^e \\ 0 & 1 \end{bmatrix} = {}_D^A\boldsymbol{T}_B^{-1} \left[{}^{\mathrm{III}}\boldsymbol{A}_{\mathrm{IV}} \boldsymbol{Rot}\left(x, -\frac{\pi}{2}\right) \right], \tag{40}$$

where ${}^{\mathrm{III}}\boldsymbol{A}_{\mathrm{IV}} = {}^{\mathrm{I}}\boldsymbol{A}_{\mathrm{III}}^{-1}\, {}^{\mathrm{I}}\boldsymbol{A}_{\mathrm{IV}}$.

Table 2. Parameters of the basic loop mechanism.

PBS-joint		Joint /Point	Theoretical position (mm)		
Parameter	Value		BUD (In $O_A - x_A y_A z_A$)	MBUG (In $O_A - x_A y_A z_A$)	ABUG (In $O_C - x_C y_C z_C$)
G_r (μm)	2~13	1	(-22.0000, -35.0000)	(-22.0000, -35.0000)	(-433.0000, -35.0000)
D_{pw} (mm)	9.5	2	(-47.8002, -141.9314)	(-57.6081, -144.4535)	(-401.1077, -143.7217)
D_w (mm)	2.381	3	(-154.0000, -35.0000)	(-154.0000, -35.0000)	(-301.0000, -35.0000)
R_i (mm)	1.226	4	(-90.8476, -320.3417)	(-118.6617, -332.1221)	(-353.3192, -306.6269)
R_e (mm)	1.238	5	(-388.4660, -1468.5658)	(-500.0000, -1440.0000)	(0.0000, -1440.0000)
D_0^j (mm) $(j=1,9)$	31	6	(-500.0000, -102.0000)	(-500.0000, -102.0000)	(0.0000, -102.0000)
		7	(-386.4324, -1493.4832)	(-500.0000, -1465.0000)	(0.0000, -1465.0000)
		8	(60.3533, -1384.7622)	(0.0000, -1398.0000)	(-455.0000, -1398.0000)
D_0^j (mm) $(j=2\sim8)$	17	9	(0.0000, -35.0000)	(0.0000, -35.0000)	(-455.0000, -35.0000)
		H	(-107.7493, -343.4932)	(-137.6426, -354.9183)	(-335.1834, -329.3716)
		B	(69.8458, -1485.7462)	(0.0000, -1500.0000)	(-455.0000, -1500.0000)
		D	(-383.1568, -1528.3297)	(-500.0000, -1500.0000)	(0.0000, -1500.0000)

where D_0^j denotes the D_0 of joint j.

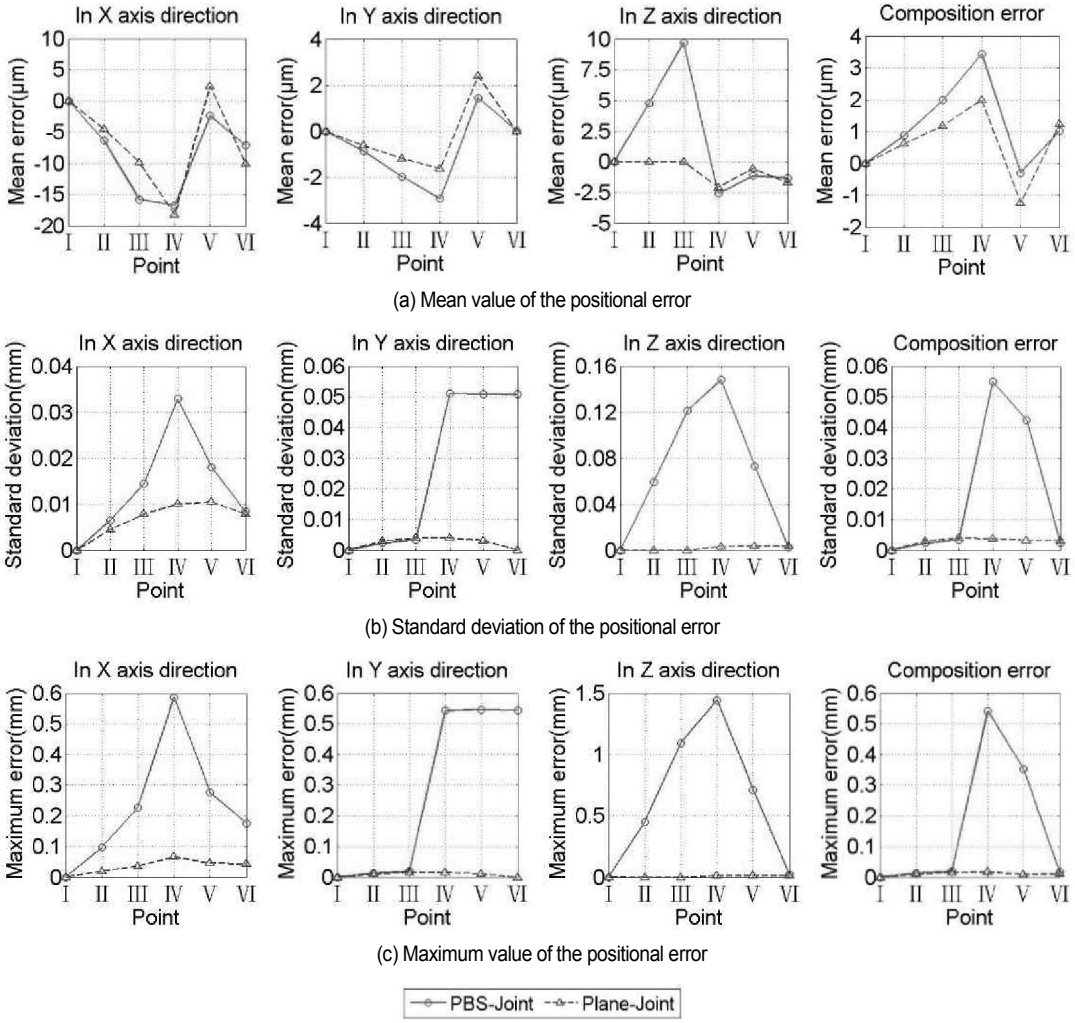

(a) Mean value of the positional error

(b) Standard deviation of the positional error

(c) Maximum value of the positional error

Fig. 18. Error distribution laws obtained by different clearance models.

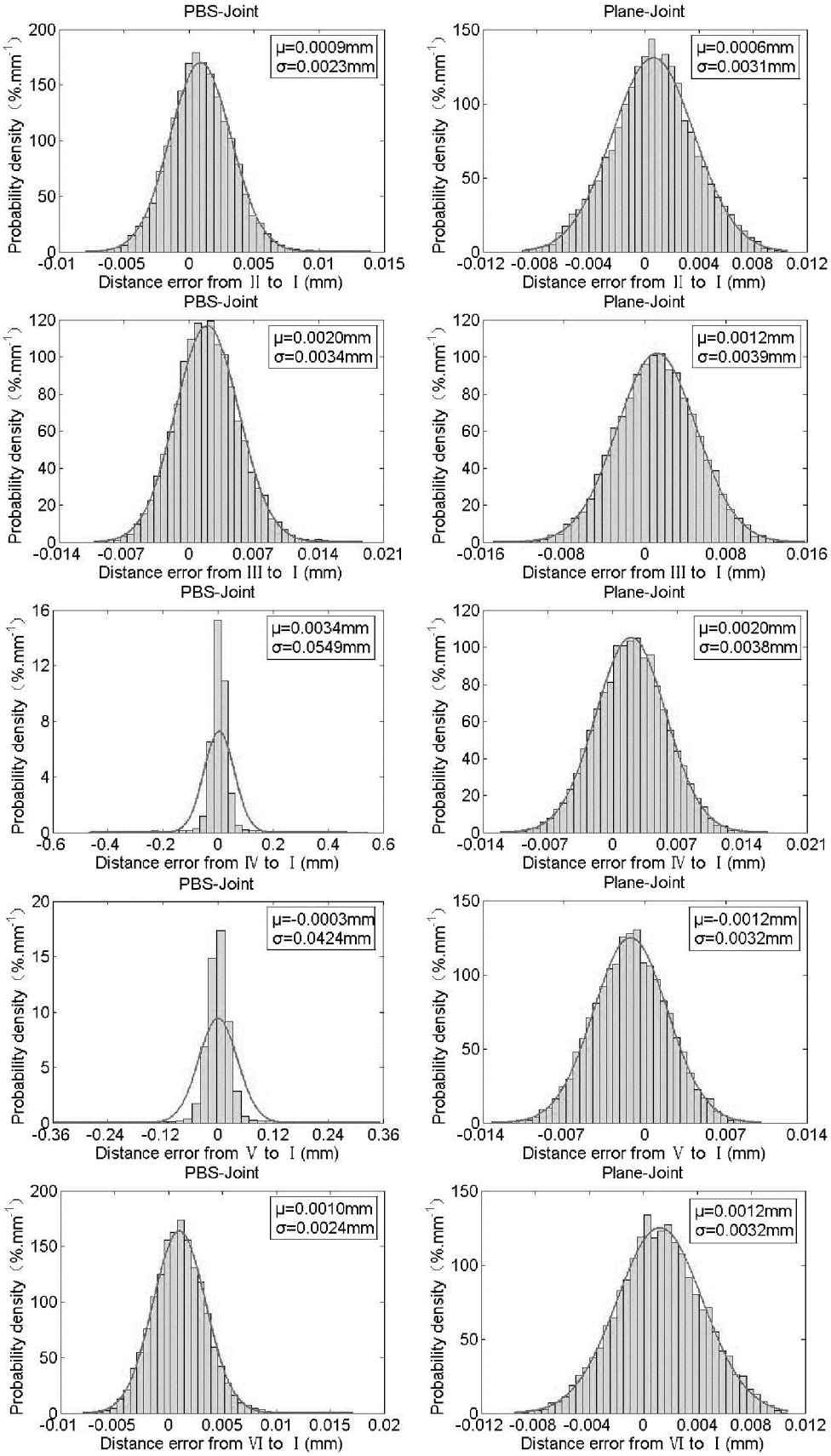

Fig. 19. Probability density distribution laws of composition error.

4.3 Analysis and discussion of results

In the basic loop mechanism, the type of all bearings is metric 628/6, and the parameters are shown in Table 2.

The deviation static selection probability of the clearance joint can be simulated and the deviation static type of each joint will be determined. Next, the parameters in the deviation calculation model of the base loop mechanism will be determined. As a result, the positional error distribution laws of the key points in mechanism can be obtained. Fig. 18 shows the positional error distribution indicators of each point obtained by simulating 10^4 times, where point I is the origin and the reference frame $O_1 - x_1y_1z_1$ as the fixed reference frame $O - XYZ$ of the basic loop mechanism. From the indicators, significant differences exist between the positional errors obtained using the PBS-joint clearance model and the plane-joint clearance model. According to the calculated result based on the two clearance models, the maximum difference of composition error (the distance error from the point to origin) appears at point IV, and the mean error, standard deviation, and maximum error calculated based on PBS-joint clearance model are 1.7, 14, and 32.3 times as much as the values calculated based on the plane-joint, respectively. Meanwhile, from the mean values of composition error, the difference between the calculated results based on the two models increases with the increase of the deviation transmission chain length.

However, although the deviation transmission chain length of points III and V are similar, from the composition errors of two models, the differences of standard deviation and maximum error at point V are 78 and 118.5 times as much as the differences at point III. Moreover, from the standard deviations and maximum errors in each direction component, the calculated results based on the two clearance models are significantly different at the Y direction of points IV, V, VI, and the Z direction of points II, III, and IV. However, the standard deviations and maximum errors of composition error only at points IV and V have significant differences.

According to the axial direction of each joint, as shown in Figs. 12 and 17, the deviation transmission paths from origin to points II, III, and VI are in plane, but the deviation transmission paths to points IV and V are in the 3D space. Therefore, the PBS-joint clearance will make the positional error of the point with a 3D deviation transmission path more widely distributed and more scattered.

Fig. 19 shows the probability density distribution of composition error. The figure also shows that the error distributions of points IV and V obtained by the two clearance models are quite different. However, for the other points, the error distributions are similar and follow the normal distribution. Therefore, for the plane mechanism, the plane-joint clearance model can be used in the analysis of the positional error. For the spatial mechanism, this model may be unsuitable. From the error distributions of points IV and V obtained by the PBS-joint clearance model, they are deviated seriously from the normal distribution law where the distributions obtained by the plane-joint clearance model still follow the normal distribution. Thus, using the plane-joint clearance model to estimate the accuracy of spatial mechanism with the PBS-joint may be meaningless.

In conclusion, for mechanisms with PBS-joint clearance, the accuracy analysis result obtained using the plane-joint clearance model may deviate from the actual situation to some extent. The longer the deviation transmission chain is, the greater the difference between the simulation results and the actual situation will be. For the spatial mechanism, the simulation results may seriously deviate from the actual situation, and the accuracy of the mechanism cannot be evaluated. Therefore, in practical engineering applications, adopting the PBS-joint clearance model, which is closer to the actual situation, is necessary in the analysis of mechanism accuracy.

5. Conclusions

A 3D clearance model of the PBS-joint was presented in this paper according to the geometric structure characteristics of the joint. With the spatial virtual link used to describe the PBS-joint clearance, the error space solution model of the serial mechanism with joint clearance on the basis of the D-H method was presented. The error space solution model of the single-loop mechanism was also obtained according to the geometric closure condition. Then, the low-layer loop sequence description method of the topological structure relations was improved, and the error space standardization solution model of the multi-loop mechanism was presented. Finally, the accuracy of the basic loop mechanism was analyzed using the plane-joint and PBS-joint clearance models. The differences of the results were addressed. The PBS-joint clearance model is helpful in analyzing the accuracy of the mechanism.

Acknowledgments

This work was supported by the National Natural Science Foundation of the People's Republic of China (Grant number 51675264) and the Natural Science Foundation of Jiangsu Province (Grant number BK20180437).

Nomenclature

PBS-joint	: Paired bearings support joint
Plane-Joint	: Plane revolute joint
3D	: Three-dimensional
BUD	: Basic unit on the directrix
MBUG	: Main basic unit on the generatrix
ABUG	: Assistant basic unit on the generatrix
CRF	: Characteristic reference frames
PCRF	: Pose characterization reference frame
G_r	: Radial clearance of bearing
$\boldsymbol{r}_{ab}$	: Vector from a to b in $O_j^{'} - x_j^{'}y_j^{'}z_j^{'}$
r_{ab}^k	: The k direction component of $\boldsymbol{r}_{ab}$
μ	: Mean value

σ : Standard deviation
${}^{j}\boldsymbol{T}_{i}$: Homogeneous transformation matrix from $O_j - x_j y_j z_j$ to $O_i - x_i y_i z_i$
${}^{j}\boldsymbol{A}_{i}$: Homogeneous transformation matrix from $O_j - x_j y_j z_j$ to $O_i - x_i y_i z_i$ after $O_i - x_i y_i z_i$ being deviated
$\boldsymbol{Rot}$: Rotation operators
$\boldsymbol{Trans}$: Translation operators
$\boldsymbol{R}$: Rotation matrix
$\boldsymbol{P}$: Position vector
$\boldsymbol{P}^{e}$: Position deviation
$\boldsymbol{\varphi}^{e}$: Attitude deviation
Θ : Error space
Γ : Error space set
III : Rank of single loop

References

[1] S. Erkaya, Effects of joint clearance on motion accuracy of robotic manipulators, *Journal of Mechanical Engineering*, 64 (2) (2018) 82-94.

[2] A. H. Chebbi, Z. Affi and L. Romdhane, Prediction of the pose errors produced by joints clearance for a 3-UPU parallel robot, *Mechanism and Machine Theory*, 44 (9) (2009) 1768-1783.

[3] G. Tibert, Deployable tensegrity structures for space applications, *Doctorial Thesis*, Department of Mechanics, Royal Institute of Technology (2002).

[4] L. Datashvili, Foldability of hinged-rod systems applicable to deployable space structures, *CEAS Space Journal*, 5 (3) (2013) 157-168.

[5] Y. Wang et al., Design and deployment analysis of modular deployable structure for large antennas, *Journal of Spacecraft & Rockets*, 52 (4) (2015) 1-11.

[6] M. W. Thomson, The Astromesh deployable reflector, *Antennas and Propagation Society International Symposium, IEEE*, 3 (1999) 1516-1519.

[7] A. Meguro et al., In-orbit deployment characteristics of large deployable antenna reflector onboard engineering test satellite VIII, *Acta Astronautica*, 65 (9) (2009) 1306-1316.

[8] S. Chodimella et al., Design evaluation of a large aperture deployable antenna, *47th AIAA/ASME/ASCE /AHS/ASC Structures, Structural Dynamics, and Materials Conference* (2006) 1603.

[9] L. Nurahmi et al., Reconfiguration analysis of a 4-RUU parallel manipulator, *Mechanism and Machine Theory*, 96 (2016) 269-289.

[10] B. Liao et al., Design and analysis of a novel parallel manipulator for pick-and-place applications, *Meccanica*, 51 (7) (2016) 1595-1606.

[11] S. J. Lee and B. J. Gilmore, The determination of the probabilistic properties of velocities and accelerations in kinematic chains with uncertainty, *ASME Journal of Mechanical Design*, 113 (3) (1991) 84-90.

[12] L. Xu and Y. Li, Modeling of a deep-groove ball bearing with waviness defects in planar multibody system, *Multibody System Dynamics*, 33 (3) (2015) 229-258.

[13] L. Xu et al., Modeling and analysis of planar multibody systems containing deep groove ball bearing with clearance, *Mechanism and Machine Theory*, 56 (2012) 69-88.

[14] Q. Zhao, J. Guo and J. Hong, Assembly accuracy prediction for planar closed-loop mechanism in view of joint clearance and redundant constraint, *Journal of Mechanical Science and Technology*, 32 (7) (2018) 3395-3405.

[15] P. Flores et al., Spatial revolute joints with clearances for dynamic analysis of multi-body systems, *Proceedings of the Institution of Mechanical Engineers*, *Part K: Journal of Multibody Dynamics*, 220 (4) (2006) 257-271.

[16] Q. Tian et al., A new model for dry and lubricated cylindrical joints with clearance in spatial flexible multibody systems, *Nonlinear Dynamics*, 64 (1-2) (2011) 25-47.

[17] C. Brutti, G. Coglitore and P. P. Valentini, Modeling 3D revolute joint with clearance and contact stiffness, *Nonlinear Dynamics*, 66 (4) (2011) 531-548.

[18] C. Pereira, A. Ramalho and J. Ambrosio, An enhanced cylindrical contact force model, *Multibody System Dynamics*, 35 (3) (2015) 277-298.

[19] F. Isaac et al., A finite element model of a 3D dry revolute joint incorporated in a multibody dynamic analysis, *Multibody System Dynamics*, 45 (3) (2019) 293-313.

[20] S. Yan, W. Xiang and L. Zhang, A comprehensive model for 3D revolute joints with clearances in mechanical systems, *Nonlinear Dynamics*, 80 (1-2) (2015) 309-328.

[21] F. Marques et al., An enhanced formulation to model spatial revolute joints with radial and axial clearances, *Mechanism and Machine Theory*, 116 (2017) 123-144.

[22] N. Akhadkar, V. Acary and B. Brogliato, Multibody systems with 3D revolute joints with clearances: An industrial case study with an experimental validation, *Multibody System Dynamics*, 42 (3) (2018) 249-282.

[23] X. Feng et al., Kinematic analysis of a PPPR spatial serial mechanism with geometric errors, *Proceedings of the Institution of Mechanical Engineers, Part C: Journal of Mechanical Engineering Science* (2018) 0954406218809124.

[24] M. Hafezipour and S. Khodaygan, An uncertainty analysis method for error reduction in end-effector of spatial robots with joint clearances and link dimension deviations, *International Journal of Computer Integrated Manufacturing*, 30 (6) (2017) 653-663.

[25] S. Erkaya, Investigation of joint clearance effects on welding robot manipulators, *Robotics and Computer-Integrated Manufacturing*, 28 (4) (2012) 449-457.

[26] S. Qu et al., Unified model for the output accuracy of open-chain manipulators that considers joint clearance and structural parameters, *Journal of Mechanical Science and Technology*, 32 (10) (2018) 4925-4931.

[27] J. Wu, X. Han and Y. Tao, Kinematic response of industrial robot with uncertain-but-bounded parameters using interval analysis method, *Journal of Mechanical Science and Technology*, 33 (1) (2019) 333-340.

[28] P. D. Lin and J. F. Chen, Accuracy analysis of planar linkages

by the matrix method, *Mechanism and Machine Theory*, 27 (5) (1992) 507-516.
[29] K. L. Ting, J. Zhu and D. Watkins, The effects of joint clearance on position and orientation deviation of linkages and manipulators, *Mechanism and Machine Theory*, 35 (3) (2000) 391-401.
[30] W. Wu and S. S. Rao, Interval approach for the modeling of tolerances and clearances in mechanism analysis, *Journal of Mechanical Design*, 126 (4) (2004) 581-592.
[31] S. Erkaya and I. Uzmay, A neural-genetic (NN-GA) approach for optimising mechanisms having joints with clearance, *Multibody System Dynamics*, 20 (1) (2008) 69-83.
[32] H. P. Jawale and H. T. Thorat, Investigation of positional error in two degree of freedom mechanism with joint clearance, *Journal of Mechanisms and Robotics*, 4 (1) (2012) 011002.
[33] A. Sardashti, H. M. Daniali and S. M. Varedi, Optimal free-defect synthesis of four-bar linkage with joint clearance using PSO algorithm, *Meccanica*, 48 (7) (2013) 1681-1693.
[34] P. Li, W. Chen and A. B. Zhu, An improved practical model for wear prediction of revolute clearance joints in crank slider mechanisms, *Science China Technological Sciences*, 56 (12) (2013) 2953-2963.
[35] W. K. Xiang, S. Z. Yan and J. N. Wu, A comprehensive method for joint wear prediction in planar mechanical systems with clearances considering complex contact conditions, *Science China Technological Sciences*, 58 (1) (2015) 86-96.
[36] D. Sun and G. Chen, Kinematic accuracy analysis of planar mechanisms with clearance involving random and epistemic uncertainty, *European Journal of Mechanics-A/Solids*, 58 (2016) 256-261.
[37] H. Tan, Y. Hu and L. Li, A continuous analysis method of planar rigid-body mechanical systems with two revolute clearance joints, *Multibody System Dynamics*, 40 (4) (2017) 347-373.
[38] Z. F. Bai et al., Reducing undesirable vibrations of planar linkage mechanism with joint clearance, *Journal of Mechanical Science and Technology*, 32 (2) (2018) 559-565.
[39] C. Innocenti, Kinematic clearance sensitivity analysis of spatial structures with revolute joints, *Transactions-American Society of Mechanical Engineers Journal of mechanical Design*, 124 (1) (2002) 52-57.
[40] G. Wu et al., Error modeling and experimental validation of a planar 3-PPR parallel manipulator with joint clearances, *Journal of Mechanisms and Robotics*, 4 (4) (2012) 041008.
[41] G. Chen, H. Wang and Z. Lin, A unified approach to the accuracy analysis of planar parallel manipulators both with input uncertainties and joint clearance, *Mechanism and Machine Theory*, 64 (2013) 1-17.
[42] K. L. Ting, K. L. Hsu and J. Wang, Clearance-induced position uncertainty of planar linkages and parallel manipulators, *Journal of Mechanisms and Robotics*, 9 (6) (2017) 061001.
[43] Z. Zhan et al., Error modelling and motion reliability analysis of a planar parallel manipulator with multiple uncertainties, *Mechanism and Machine Theory*, 124 (2018) 55-72.
[44] M. Domaneschi, Experimental and numerical study of standard impact tests on polypropylene pipes with brittle behaviour, *Proceedings of the Institution of Mechanical Engineers, Part B: Journal of Engineering Manufacture*, 226 (12) (2012) 2035-2046.
[45] M. J. Tsai and T. H. Lai, Accuracy analysis of a multi-loop linkage with joint clearances, *Mechanism and Machine Theory*, 43 (9) (2008) 1141-1157.
[46] S. Erkaya, Trajectory optimization of a walking mechanism having revolute joints with clearance using ANFIS approach, *Nonlinear Dynamics*, 71 (1-2) (2013) 75-91.
[47] X. Zhang and X. Zhang, A comparative study of planar 3-RRR and 4-RRR mechanisms with joint clearances, *Robotics and Computer-Integrated Manufacturing*, 40 (2016) 24-33.
[48] X. Zhang and X. Zhang, Minimizing the influence of revolute joint clearance using the planar redundantly actuated mechanism, *Robotics and Computer-Integrated Manufacturing*, 46 (2017) 104-113.
[49] F. Lin et al., Deployment accuracy analysis of cable-strut deployable mechanism with joint clearances and forces constrained, *Journal of Vibroengineering*, 20 (5) (2018) 2085-2098.
[50] X. Li, X. Ding and G. S. Chirikjian, Analysis of angular-error uncertainty in planar multiple-loop structures with joint clearances, *Mechanism and Machine Theory*, 91 (2015) 69-85.
[51] Q. Zhao et al., Analysis of angular errors of the planar multi-closed-loop deployable mechanism with link deviations and revolute joint clearances, *Aerospace Science and Technology*, 87 (2019) 25-36.
[52] Q. Zhao et al., Deviation propagation analysis and accuracy modeling for multi-closed-loop mechanism, *Journal of Mechanical Engineering*, 54 (21) (2018) 170-179.
[53] R. P. Paul, *Robot Manipulators: Mathematics, Programming, and Control: The Computer Control of Robot Manipulators*, Richard Paul (1981).
[54] J. Denavit, A kinematic notation for lower-pair mechanisms based on matrices, *Trans. of the ASME. Journal of Applied Mechanics*, 22 (77) (1955) 215-221.

Fei Lin received his Masters degree in Machinery and Electronics Engineering from the Jiangxi University of Science and Technology, China, in 2013. At present, he is pursuing a Ph.D. in Aerospace Science and Technology from Nanjing University of Aeronautics and Astronautics. His current research interests include spacecraft structure and mechanism design and nonlinear stochastic dynamics.

Chuanzhi Chen holds a Ph.D. in Aerospace Science and Technology from Nanjing University of Aeronautics and Astronautics. His research interests include low-impact docking mechanism, spacecraft structure and institutions, and structure dynamics of spacecraft.

Jinbao Chen holds a Ph.D. in Aerospace Science and Technology from Nanjing University of Aeronautics and Astronautics. His research interests include structure dynamics of spacecraft, spacecraft structure, and mechanism design.

Meng Chen obtained his Ph.D. in Mechanical Design and Theory from the Huazhong University of Science and Technology, China, in 2003. Currently, he is a Deputy Chief Engineer at Aerospace Systems Engineering Shanghai, China. His research interests include structure dynamics of spacecraft, spacecraft structure, and mechanism design.